JOINT EUROPEAN TORUS JET

JET–P(90)44

V.P. Bhatnagar, J. Jacquinot, B.J.D. Tubbing, D. Stork, A. Tanga, B. Balet, G. Bosia, M. Bures, D. Campbell, S. Clernent, A. Hatayarna, K. Lawson, F. Tibone, D.F.H. Start and JET Team

ICRH Produced H-Modes in the JET Tokamak

ICRH Produced H-Modes in the JET Tokamak

V.P. Bhatnagar, J. Jacquinot, B.J.D. Tubbing, D. Stork, A. Tanga, B. Balet, G. Bosia, M. Bures, D. Campbell, S. Clernent, A. Hatayarna[1], K. Lawson[2], F. Tibone, D.F.H. Start and JET Team*

JET-Joint Undertaking, Culham Science Centre, OX14 3DB, Abingdon, UK

[1]Toshiba Corporation Chome, Chiyoda-Ku, Tokyo, Japan
[2]UKAEA Culham Laboratory, Abingdon, Oxon, OX14 3DB
** See Appendix 1*

Preprint of Paper to be submitted for publication in
Plasma Physics and Controlled Fusion

Table of Contents

ABSTRACT.

H-modes produced by the ion-cyclotron resonace heating (JCRH) in a double-null Xpoint open-divertor configuration in the JET tokamak are studied where the ICRH antennas, operated in the dipole $(0, \pi)$ phasing, are located on the low-field side of the tokamak. The beryllium evaporation on the nickel antenna screen and the first wall of the tokamak have played a crucial role in achieving H-modes with ICRH alone. These H-modes have a duration of up to 1.5s with an ICRH power level of up to 12MW. In these discharges, all characteristics typical of neutral-beam injection heating H-modes are found and the global energy confinement time approaches two-times the Goldston L-mode prediction. For most of their duration, ICRH Hmodes are free from ELMs (edge localized modes). In addition, the monster sawtooth (long sawtooth free period) feature of ICRH is maintained during H-modes leading to central electron temperature (T_{e0}) of 10keV nearly twice the value of central ion temperature (T_{i0}). In NBI heating H-modes, the T_{e0} is generally lower than the T_{i0}, but the combined ICRH + NBI heating H-modes allow both T_{e0} and T_{i0} close to 10keV simultaneously. The elevated T_{e0} by ICRH in the combined heating increases the slowing down time of beam ions and increases the D-D reaction rate and the neutron output. ICRH H-modes often occur as a two-step transition and the antenna plasma coupling resistance (R_c) also decreases in two-steps. Theoretical values of R_c agree well with experimental values during the H-phase.

1.0 INTRODUCTION :

Since the first demonstration of H-mode (high-confinement mode) in 1982 in ASDEX in a magnetic divertor configuration using neutral-beam injection (NBI) heating, H-modes are now routinely produced with practically any type (or a combination) of additional heating in most tokamaks that can operate either in a closed divertor configuration such as ASDEX (Wagner et al, 1982, Keilhacker et al, 1984), JT-60 (Akiba et al, 1988), or in an open divertor configuration such as JFT2-M (Matsumoto et al, 1987), DIIID (Ohyabu et al, 1985), JET (Tanga et al, 1986) etc. Some other references can be found in a review paper (ASDEX Team, 1989). In the proposed next-step devices such as NET/ITER (ITER Team, 1989) ion-cyclotron resonance heating (ICRH) is the most promising alternative to NBI heating in which for good penetration to the core of the reactor plasma, beam energies in the MeV range are required that at present necessitates considerable development work. But, ion cyclotron resonace heating deposits RF power centrally in a high-density plamsa and it has a good potential for current-drive in a reactor for its steady state operation. Therefore, it is of particular importance that H-modes can be produced by this heating method. Short duration H-modes with ICRH at the second harmonic were first produced in ASDEX (Steinmetz et al, 1986; Steinmetz et al, 1987). H-modes longer than the energy confinement time were observed in JFT-2M (Matsumoto et al, 1987) where the ICRH antennas were located on the high-field side which are apparently well suited from the H-mode view-point, as the antennas see a lower plasma power load which aids in keeping the plasma edge relatively undisturbed.

In JET (as in most other tokamaks), ICRH antennas are located on the low-field side where space is more readily available. The early operation was carried out in JET with carbon limiters and carbonized nickel antenna screen which led to an increased influx of neutral gas and impurities (Bures et al, 1988a). This tends to impair the edge conditions that are crucial to the production and maintenance of an H-mode. Helium glow-discharge cleaning was also used but, the H-modes with ICRH could not be produced due to specific ICRH impurity effects such as enhanced nickel influx from the electrostatic screen of the powered antenna. However, this problem of the specific ICRH impurity effects and the edge perturbation could be satisfactorily alleviated to produce H-modes with ICRH as follows:

(1) Beryllium gettering is applied to the nickel screen and the first-wall of the tokamak,

(2) The antenna is used in the dipole $(0, \pi)$ phasing,

(3) The antenna screen blades are inclined at 15 deg. (from the toroidal direction) to align them approximately with the total magnetic field.

Also, a fast automatic-matching system (Bosia et al, 1989) based on slight frequency changes together with a slower adjustment of mechanical stubs is incorporated to cope with changes of antenna-plasma coupling at the transition and during the H-mode. This system has the capability to remain in a reasonably good match as a function of time during a shot when the coupling resistance changes due to changes in the edge-plasma conditions at the transition. This permits to maintain a certain level of power delivered to the plasma by the ICRH system which otherwise would suffer severely from voltage breakdown and tripping of the generator.

We must point out that the above conditions are found to be sufficient to produce an ICRH H-mode but they may not be absolutely necessary and further experimental investigations are being carried out to relax the above conditions. For example, H-modes with monopole (0,0) phasing have not yet been obtained with RF alone but gave good results in combination with NBI. Monopole phasing is of interest due to its higher coupling resistance and better power coupling capability for a given voltage stand-off in the antenna and the transmission line.

An understanding of the impurity influx from the antenna screen due to ICRH has played a significant role in successfully obtaining an H-mode with ICRH. The beneficial effect of the $(0, \pi)$ phasing in achieving lower impurity condition has previously been observed in many experiments as, for example, JFT-2M (Tamai et al, 1986), JET (Bures et al, 1988b), TEXTOR (Messiaen et al, 1989) and TFTR (Stevens et al, 1990). Also, the reduction in plasma-wall interaction during ICRH by appropriate wall-conditioning such as 'carbonization' and 'boronization' has been discussed by Messiaen (Messiaen et al, 1986). Further, in JET the observed scaling of the impurity release from the screen of an ICRH antenna (see Fig. 1) is found to be compatible with a sputtering mechanism due to the RF sheath rectification of the applied RF voltage (see Fig. 2), in combination with the coventional Bohm sheath, which provides a large dc potential drop in which ions accelerate and cause sputtering (Perkins, 1989). This potential drop is a nonlinear function of plasma density at the antenna screen (Myra et al, 1989) which goes to zero at low density and saturates at high densities. There are two ways that these sheaths can be produced. "Short-length" (D'Ippolito et al 1989) gap-sheaths (field line crossing between the antenna blades), see Fig. 1 (a), and the "long-length" (Jacquinot, 1989a) front-surface sheaths (between the contact points of the field line on the two sides of the antenna) can be formed (see Fig.1 (b)). The deleterious effect of

the former is eliminated by aligning the screen to the field line and the latter is made ineffective due to the out of phase operation in the dipole mode (net voltage is zero toroidally). In the case of misalignment, effect of self-sputtering which is the dominant cause of impurity influx is reduced by beryllium coating for which self-sputtering coefficient is less than unity for perpendicular incidence (Roth et al, 1987). Further, there is a strong Be-gettering which reduces oxygen concentration, ($<0.1\%$) as well as there is a significant reduction of sputtering caused by oxygen ions themselves. Moreover, beryllium environment allows a strong pumping and lowers the influx of neutrals thus reducing recycling. Also, it permits extra gas puffs thus further screening the impurities from the plasma. The duration of H-modes is also longer (in ICRH or other combined scenarios) as the radiated power is smaller in the Be environment.

As mentioned above, H-modes have not yet been obtained with monopole operation of ICRH alone as it suffers from the front-surface sheath effects and produces higher influx of impurities as compared to the dipole operation (Bures et al, 1989). But, the deleterious effects of this phasing do not seem to be dominant in H-modes obtained with combined ICRH + NBI heating where we take advantage of better coupling and higher RF power coupled with monopole.

In this paper, evidence will be presented that demonstrates that ICRH produced H-mode discharges in the JET tokamak have the same signatures as those found in the NBI H-mode discharges and the energy confinement time is close to two-times the Goldston L-mode (Goldston, 1984) prediction. Based on a TRANSP analysis (Goldston et al, 1981) the improvement in confinement is found to be due to a reduction in heat-diffusivity in the plasam edge region as compared to an L-mode discharge. For most of their duration, ICRH H-mode discharges are found to be free from edge-localized modes (ELMs). These discharges feature higher electron temperature and are accompanied by monster sawteeth (ultra-long sawteeth (Campbell et al, 1988) with a duration greater than the energy confinement time) that are a characteristic of the minority ion cyclotron heating scheme. The ion temperature is generally lower than the electron temperature but nevertheless it is higher in H-phase as compared to the L-phase. The DD-reaction rate also goes up in the H-phase. Further, the two heating schemes ICRH and NBI are complimentary to each other as ICRH heats electrons via strong minority ion tail whereas NBI relaxes mostly on the background ions. Therefore, in H-modes produced by the combined ICRH + NBI heating both electron and ion temperatures close to 10 keV are obtained simultaneously concomitant with the H-mode confinement.

The paper is organised as follows. In Section 2.1, first we briefly outline the experimental conditions and plasma configuration used to produce H-mode discharges with ICRH. In Section 2.2, we present time traces of signals that show the characteristic signature of H-mode discharges obtained by ICRH alone and those with combined heating. In Section 2.3, we present another characterization

of H-mode discharges in terms of edge-density and edge-temperature. In Section 2.4, we present the energy confinement data obtained in different H-mode scenarios and compare them with a popular yard-stick of confinement that was deduced from NBI L-mode tokamak discharges by Goldston (Goldston et al, 1984). The results of a local transport analysis of an ICRH H-mode is also presented in this section. Electron and ion heating observed in different schemes of producing H-mode discharges is presented in Section 2.5. Further, in Section 2.6, we illustrate the behaviour of impurities observed spectroscopically and discuss their contribution to the radiated power in an ICRH H-mode discharge. In Section 3, we discuss the behaviour of the change of antenna loading at an L-H transition and the associated problem of generator impedance matching. Further in this section, the behaviour of the ICRH antenna coupling resistance in the H-mode discharges is presented and a comparison is made from the results that are predicted theoretically from an antenna plasma coupling code. Discussion and conclusions of this study are contained in Section 4.

2.0 EXPERIMENTAL RESULTS :

2.1 Experimental Setup.

JET (Joint European Torus) is a D-shaped large tokamak (Rebut et al, 1984) with major radius R_0 = 2.96 m, minor radius a_p = 1.2 m, nominal toroidal field B_t = 3.4 T, plasma current I_p = 5 MA (upgraded to 7 MA), and plasma elongation = 1.6. For the results presented in this paper, the plasma current was 3 MA, toroidal field = 2.8 T and the RF frequency of operation = 43 MHz. The plasma composition was hydrogen minority (≅ 2-4%) in deuterium majority gas. The JET ICRH system has been described previously (Wade,1985 ; Kaye, 1987). There are eight antennas (see Kaye, 1987) which are symmetrically distributed around the torus. A sketch of the A1-antenna layout is shown in Fig. 1. A JET antenna has essentially two radiating elements that are separated toroidally which can be driven in phase (monopole) or out of phase (dipole). ICRH power is delivered to the plasma by coupling the fast magnetosonic wave which deposits its power mainly via the minority-ion cyclotron damping in a narrow region (about 30 cm) near the ion-ion hybrid resonance zone (Jacquinot, 1986). Deuterium was also used in the NBI system which has two injection boxes one with 80 keV and the other with 140 keV beams that are injected in which a part is nearly perendicular and the other part is nearly tangential in the co-direction (see Deusing et al, 1986).

In this paper, we include the data obtained in double-null X-point discharges with ICRH alone, NBI alone and combined ICRH + NBI heating experiments. See Fig. 3 for an illustration of the double-null configuration obtained from the IDENTC equilibrium-code (Lazzaro et al, 1987) which reconstructs the plasma flux-surfaces from the measurements made by a series of coils located close to the vacuum-vessel wall. This configuration allows to match the plasma shape poloidally to the antenna surface for improved coupling of the antenna to plasma. Also, the plasma was brought very close to the midplane antenna side-protection tiles (≅ 2 cm) and still produced an H-mode successfully. Generally, the dominant power load is found to be on the top X-point possibly due to the slight asymmetries in the magnetic system. In these experiments, grad-B drift of ions is also towards the top. Note that the X-point target tiles are made of carbon and are radiation cooled. The inner wall is also covered by carbon protection tiles.

The JET vacuum vessel is made of inconel. There are two toroidal belt limiters on the low field side (see Fig. 3). For the early experiments they were made out of carbon but later replaced by beryllium. The first wall of the tokamak and the nickel screen of the antenna are subjected to a beryllium coating by an in-situ evaporation of beryllium. In the results presented in this paper, we do not distinguish between the two types of belt limiters as limiters play only a minor role in the X-point discharges. Further, Be evaporation was used in both experiments by which carbon limiters were also covered by a beryllium coating. A comparison of the results of limiter discharges with the two types of limiter material is given by Dietz (Dietz et al, 1990).

For general tokamak diagnostic systems including that of JET see, for example, a review paper (Orlinskij and Magyar, 1988 and references therein). In the data presented here, the electron density and its profile was measured by a multi-channel far infra-red interferometer. The profiles of electron density and temperature were also determined by a LIDAR (LIght Detection And Ranging) Thomson scattering system at some fixed time-slices. The electron temperature profiles were measured by electron-cyclotron emission diagnostics and the ion temperature in the central region was measured by Doppler broadening of the Ni-XXVII spectral line by a high resolution X-ray crystal spectroscopy technique. In the presence of NBI, the ion temperature and its profile was also measured by charge-exchange recombination (CXR) spectroscopy. The relative density scrape-off lengths are estimated from a series of Langmuir probes that are located in the X-point region. The data from these probes for the present experiments was available only for fixed-bias operation and therefore estimates of the e-folding lengths of ion satuaration currents only are available in the X-point region. In the absence of measurements in the midplane near the antenna, the data at the X-point may eventually be transformed to mid-plane by taking account of the compression of flux there. The antenna plasma distances are obtained from IDENTC equilibrium-code mentioned above.

2.2 *Typical Time Traces of H-Mode Discharges.*

2.2.1 An H-mode With ICRH Alone.

In H-modes produced by ICRH alone, all characteristics typical of H-mode discharges are found (see Fig. 4). At the transition from L to H-phase, one can see a sudden drop in D_α emission, a small decrease and then a gradual increase in the radiated power (P_{rad}) from the plasma, increase in the plasma density and more importantly an increase in the slope of stored energy (W_{DIA}, for example) at a constant power level. Also there is an increase in the ion temperature (T_{i0}) and DD reaction rate (R_{DD}) which eventually decreases due to increase in Z_{eff} or dilution. Further, there is an increase in the edge-density gradient (or a reduction in scrape-off length (SOL), not shown), which results in a decrease of coupling resistance R_c. There is a slight increase in the distance from the plasma separtrix and the antenna side protection tiles D_{ap} but this increase is generally not enough to account for the decrease of R_c (see Section 3). Often, P_{RF} reduces after the transition to H-mode due to the decrease of R_c and tripping of some of the generators caused by the voltage-breakdown in the antenna and/or the transmission line. Note that in this shot P_{RF} was reduced in anticipation but the stored energy did not decrease significantly practically until the H-mode was terminated when P_{RAD} reached the input power level. This effect of hysteresis is well known for H-mode discharges where the H-phase can be maintained at a lower power level than what was necessary for the transition. The global energy confinement in this situation was $\cong$ 1 s for a flat top RF pulse of about 1 s. It can be seen that for most of the H-phase the D_α signal is ELM free. Also, there is a clear reduction of noise on the coupling resistance trace during the H-phase which could be related to the reduced fluctuations on the edge density, but no quantitative data is available at present. Efforts are being made to make the fluctuation measurements by microwave reflectometer diagnostics (Prentice et al, 1990).

As will be shown in Section 2.3, the transition from L to H-phase is found to occur when a certain electron temperature at the edge is reached at a given density and a pedestal has been formed (Keilhacker et al, 1986). In NBI produced discharges, often the transition is triggered by the crash of a sawtooth which leads to the propagation of a heat pulse which increases the edge temperature necessary for the transition to an H-mode. However, in ICRH discharges where sawteeth are stabilized (see below), this mechanism of trigger is absent. The transition should therefore occur only after a delay from the start of the RF pulse where the heat deposited by the ICRH at the center diffuses out and elevates the edge temperature. In ICRH H-modes discharges, this delay is about 400-500 ms. In some discharges, the ICRH pulse was switched on before

the X-point was formed to prevent the density from falling too low. In NBI H-modes, the transition has been found to occur after a delay of only 200 ms but aided by the crash of a sawtooth. The required threshold power for the transition is about 8 MW at B_T = 2.8 T which is roughly the case with NBI H-modes also. A detailed study of the parametric dependance of the threshold power in ICRH H-modes has not yet been done. Further, it is found that the transition in NBI H-Modes is completed more rapidly (10-20 ms) whereas in ICRH H-modes, this duration is 60-80 ms.

2.2.2 An ICRH H-mode with a Two-Step Transition.

In H-modes produced by ICRH, we have found that in some discharges the transition occurs in a single step (as shown in Fig. 4) but, in some other discharges it occurs in two steps that are separated by about 0.5 s. In Fig. 5, we show an example of such a discharge in which the L-H transition takes place in two steps as is evident from the $D\alpha$ trace. Correspondingly, there are dips in the radiated power signal. As will be shown in Section 3, antenna coupling resistance also decreases in two steps which is correlated with the characteristic steepening of the edge-density profile in H-modes discharges and is consistent with a relative decrease of ion saturation currents measured by Langmuir probes located in the low-field side of the X-point region. The physical mechanism for such a two-step transition is not yet clear. In this discharge, the Z_{eff} measured by visible Bremstrahlung remains close to a value of 2.5 during the entire H-phase. Also, note from the electron temperature trace that the sawtooth-free periods (monster sawtooth) created by ICRH are not lost at the transition and their duration in ICRH H-modes has been found to be be as long as 1.3 s.

2.2.3 An H-mode With Combined ICRH + NBI heating.

Now we show the time traces of a discharge in which the H-mode was obtained by the combined ICRH + NBI heating in which the ICRH was applied at about 1 s after the NBI heating pulse (see Fig. 6). ICRH power was increased with a ramp of about 1 s. The transition to H-mode occured when the ICRH power reached its flat top value as is evidenced from the $D\alpha$ trace. In this case we find that the H-phase is somewhat ELMy. But in this case, (as compared to the case above) even longer sawtooth-free periods are obtained ($\cong$2.5 s) where monopole can be used which facilitates obtaining the monster sawtooth (see Fig. 6). It can be seen that the monster sawtooth was also started by the ICRH and it lasted practically the entire length of the RF pulse. It has been an experimental observation that a monopole creates a monster sawtooth more easily than a

dipole. By virtue of the difference in their excited $k_{//}$-spectrum, this observation may be related to the more peaked power deposition in the monopole and more power being deposited in the minority ions thus creating stronger tails. Here, $k_{//}$ refers to the wave propagation constant parallel to the equilibrium magnetic field.

The electron temperature reaches about 12 kev and T_i measured by Doppler broadening of Ni-XXVII line is about 8 keV which is an underestimate when the electron temperature is greater than 8 keV. This is related to the ionization potential of the line and in this case the dominant contribution to the signal is from slightly off-axis and the central temperature would be higher. Indeed, the T_{io} measured by CXR spectroscopy gives a value of $\cong$ 10 keV.

Also, note that there is an eigen mode structure (McCarthy et al, 1988) in the trace of the coupling resistance which is a general charateristic of the fast-wave heating by a monopole antenna. The eigen modes in the monopole antenna which has a k// spectrum centered at zero with a half width of $\cong$ 4.5 m^{-1} are produced due to weak damping. They are radial eigen modes and are interpreted as standing waves between the fast-wave mode conversion/cutoff layer in the plasma and the cutoff layer at the edge. The eigen modes occur when the distance between the two cutoff layers is a multiple of half-wavelength. For $k// = 0$, the wavelength in the radial direction is given by

$$k_{perp} = k_0 \, \omega_{pi}/\omega_{ci}$$

where k_{perp} is the wave number in the radial direction, k_0 is the propagation constant in vacuum, ω_{pi} is the majority species ion plasma frequency and ω_{ci} is the ion cyclotron frequency. Therefore, a series of resonance are expected when, for example, the density is varied as seen in Fig. 6. Further, note that the spacing of the resonances as a function of time is well correlated to the rate of change of density at the slower rise and faster fall of the density during the RF pulse.

2.3 Edge-Density, Edge-Temperature Behaviour of H-Mode Discharges.

Another characteristic of H-mode discharges has been studied by observing the behaviour of edge temperature (T_{es}) as a function of edge density (n_{es}) as the plasma travels through the time domain from L to H-phase and then back to L-phase (Bhatnagar et al, 1987). For convenience, the presently available outermost density interferometer channel located at a major radius R = 3.75 m is used which is not exactly at the edge but it is in the profile about 30 cm from

the edge whereas the plasma diameter in the horizontal direction is about 2.3 m. At the corresponding radius, the electron temperature measured by ECE, T_{es}, is then plotted aginst the n_{es} as shown in Fig. 7 where time is the parameter along the curves. Two shots are shown, an NBI H-mode and an ICRH H-mode. The solid circles and the hatched circles represent the L-H and H-L transitions respectively. It is seen that L-H transitions take place at higher temperature and lower density after which the discharge remains in H-mode and finally reverts back to L-mode at lower temperature and higher density at the edge. To further elucidate the point, the values of T_{es} and n_{es} taken at the L-H and H-L transitions are plotted in the T_{es}, n_{es}-plane for a series of H-mode discharges both obtained by NBI and ICRF heating as shown in Fig. 8. The data points separate the H-mode region from the L-mode region as indicated and there is a certain overlapping of the two regions due to a scatter in the data. The B_T = 2 T, I_P = 2 MA points are an earlier data that was obtained without the Be-evaporation whereas 2.8 T, 3 MA data was obtained with Be-evapoartion. ICRH and NBI data points have been identified which shows that the behaviour of the two is very similar. This figure clearly delineates the operational regime of L and H-phases of the discharge in the JET tokamak. Similar results were found when the data was available from another previously available outermost density channel that was located 20 cm from the edge of the plasma. From this figure, it appears that the product of T_{es} and n_{es} (or the electron pressure) at the edge may be an important parameter in distinguishing L from H-phase rather than the T_{es} or n_{es} alone. Also, we note that in this characterisation, we do not find any appreciable difference in the data of 2 T, 2MA and that of 2.8 T, 3 MA.

2.4 Confinement Properties of H-mode discharges.

2.4.1 Global Energy Confinement.

A plot of stored energy W (from diamagnetic-loop measurement) plotted as a function of P_T-dW/dt for a series of JET discharges at I_P = 3 MA for several different scenarios is shown in Fig. 9. The data points have been identified, as indicated in the inset, for H-mode discharges with ICRH, NBI, and combined ICRH+NBI. Also some NBI ELMy H-mode points have been shown for comparison. We also present the L-mode confinement data obtained with ICRH alone and NBI alone as indicated in the figure. The global energy confinement time τ_E is defined as the ratio of $W/(P_T\text{-}dW/dt)$ where the effect of radiated power is neglected as it predominantly comes from the edge of the plasma. The value of τ_E can be readily obtained from the data points in the figure. The three broken lines on the figure represent the Goldston L-mode prediction W_G (Goldston,

1984), $1.5W_G$ and $2W_G$ respectively for such discharges. The NBI heated limiter-plasma agree well with the Goldston prediction as this scaling indeed was deduced based on such discharges from a number of tokamaks. ICRF heated L-mode double-null X-point discharges lie between W_G and $1.5W_G$-line and follow the usual off-set linear behaviour for such discharges with an incremental confinement time (Bhatnagar et al, 1989a) τ_{inc} = 0.34 s deduced from the slope of the line through the ICRH L-mode data points. The difference in ICRH and NBI L-mode points comes partly from the off-axis power deposition in these NBI discharges in JET whereas the ICRH deposits power centrally. But, the main difference is due to the fact that in the ICRH discharges, there is a larger fast-ion contribution as compared to NBI heating. In the case of NBI heating in JET, the injected beam ions mostly relax on the plasma ions and the beam is considerably more isotropic whereas the ICRF minority ion heating produces relatively strong perpendicular energy tail which is well confined in JET and, it relaxes on electrons. In the latter case, the fast ion energy can be inferred from W_{DIA} and W_{MHD} (equilibrium identification code) and it is about 10-30%. In the former case, there is no experimental measurement except from NBI power deposition codes and for the data presented, it is about 5-15%. In H-mode discharges, due to higher density which generally accompanies the H-phase, the fast ion contribution is small. We find that the H-mode data obtained by NBI, ICRH and combined ICRH + NBI is about the same and lie between $1.7\text{-}2.2W_G$. In some of the ICRH discharges, due to a certain hystersis effect such as shown in Fig. 4, the confinement time at lower power appears to be noticeably higher.

2.4.2 Local Transport Analysis.

We use a time-dependent transport analysis code TRANSP (Goldston et al, 1981) which solves the equilibrium and magnetic field diffusion equations and then using the particle and energy conservation equations calculates the local transport coefficients. The input data to the code includes electron temperature profile, ion temperature profile (when available), electron density, Z_{eff} and radiated power profiles and the edge particle confinement times from D_α-monitors. The ICRH power depostion profiles are calculated using the ray-tracing code BRAYCO (Bhatnagar et al, 1984) which is based on a full analysis of the finite antenna geometry, its full radiation spectrum and hot-plasma damping in a D-shaped tokamak plasma. The data used in this analysis are checked for consistency by verifying that the calculated stored energy, the surface voltage, and the total neutron yield are within the experimental uncertainties of the values measured experimentally.

For the additional heating experiments carried out with ICRH alone, the charge-exchange recombination spectroscopy measured ion-temperature profiles

are not available. The profile has been modelled with an ion thermal diffusitivity (χ_i) proportional to the electron thermal diffusitvity (χ_e). The constant of proportionality is adjusted as a function of time such that the calculated central ion temperature matches that measured experimentally by Doppler-broadening of Ni-XXVII line observed with X-ray crystal spectrometer. Under this limitation where the χ_e and χ_i can not be determined independently, here we present the results in terms of an "effective" thermal diffusivity defined as

$$\chi_{eff} = \frac{(\chi_i n_i \nabla T_i + \chi_e n_e \nabla T_e)}{(n_i \nabla T_i + n_e \nabla T_e)} \qquad (1)$$

where n_e, n_i, T_e and T_i are electron and ion densities and electron and ion temperatures respectively. The results of the TRANSP calculated χ_{eff} as a function of the normalized flux coordinate ρ (where $\rho = 1$ at the plasma boundary and $\rho = 0$ at the magnetic axis) are shown in Fig. 10 for an ICRH produced H-mode and they are compared to that obtained in an ICRH L-mode but which had a monster sawtooth (Balet et al, 1990). It is found that in the case of an L-mode discharge χ_{eff} increases nonlinearly as a function of ρ whereas in the case of an ICRH H-mode χ_{eff} decreases in the outer regions of the plasma improving the confinement in the edge plasma. This could be correlated to the steepening of the denisty profile in that region during the H-phase of the discharge. The error bars reflect the errors in ∇T_i, ∇T_e and those in the power deposition profiles.

2.5 *Electron and Ion Heating.*

Central ion temperature T_{i0} (Doppler-broadening of Ni-XXVII line) and electron temperature T_{e0} (ECE) are plotted in Fig. 11-12 as a function of $P_{TOT}/\langle n_e \rangle$ (volume average) for the data set used above. For ICRF heated L and H-modes, the T_{i0} is generally low (4-6 keV) and is a general characteristic of the minority heating. Dipole phasing was used in these discharges, but in JET similar behaviour of T_i is also found with monopole in non H-mode ICRH discharges (Bhatnagar et al, 1989b). In the case of NBI or ICRH + NBI heating, beam ions relax on plasma ions and heat them preferentially leading to a linearly increasing T_{i0} with $P_{TOT}/\langle n_e \rangle$. Since in ICRF heating, a strong minority-ion tail is produced which dominantly interacts with electrons, higher T_{e0} values are obtained for ICRH data as shown in Fig. 12. In NBI shots, electron heating is generally poor, but in H-modes with combined heating ($P_{RF}/P_{NBI} = 0.4$-0.8), ICRH pushes the T_{e0} to highest values. Thus as expected, H-modes with combined heating, allow high values of both T_{e0} and $T_{i0} \cong 10$ keV together with the H-mode confinement. We must point out that to link the data given in Fig. 11 and 12 to

energy confinement time, appropriate plasma volume and profiles of T_i, T_e, n_e and Z_{eff} (effective charge) must be taken into account.

The importance of ICRH in elevating the electron temperature during NBI heating lies in the fact that the higher electron temperature increases the slowing down time of the beam ions thus increasing the stacking factor (a larger number of fast ions in the plasma) and leading to increased neutron yield (see R_{DD} trace in Fig. 6). A part of the increased neutron yield in the combined heating experiments also comes from the second harmonic heating of the beam ions as evidenced from the neutron energy spectra (Sadler et al, 1990) which show a deuterium tail at energies higher than the beam injection energies. We must point out that RF produced tails of protons or deuterons can also interact with Be-impurity ions (Sadler et al, 1990) leading to the generation of neutrons via $^{9}Be(p,n)^{9}B$ and $^{9}Be(d,n)^{10}B$ reactions. However, in the double-null X-point discharges used here, where the X-point protection tiles are in carbon, the Be-concentration in the discharge is much lower than that of carbon and nickel impurities (see next section) and the neutrons produced by these reactions are likely to be small. The neutrons produced in the ICRH H-mode discharges are found to be a factor of about 2 higher than those obtained in L-mode discharges (Jacquinot et al, 1989b) and roughly correspond to the neutron yield achieved in peaked density profile discharges heated by ICRH alone at similar power levels. Further, we point out that the electron temperature profiles in the case of H-modes with ICRH alone are more peaked than those that are found in the NBI H-mode discharges. However, the electron density profiles at the transition to an H-mode steepens at the edge and becomes very flat over the cross section in both cases. But, in the case of NBI they can sometimes be hollow (Gowers et al, 1988).

2.6 Impurity Behaviour during an ICRH H-mode.

In Fig. 13, we show the total radiated power as measured by an array of bolometers (which also view the X-point region) for an H-mode discharge produced by ICRH alone. The L-H transition occurs at about 10.3 s where as usual there is a dip in the radiated power trace. The H-mode is generally terminated as in the NBI case when the radiated power exceeds a certain value which in this case is about 60% of the input power. The duration of the monster sawtooth is schematically noted on the figure. The monster sawtooth started in the ramp up phase of the RF pulse and lasted through the H-phase giving a peak in the radiated power at its crash. In this particular shot, the plasma touched the antenna side-protection tiles inadvertantly near the midplane at $t = 12.3$ s which led to an increase in density and radiated power after this time as opposed to

other H-mode shots where the radiated power decreases after the H-phase. The spikes on the radiated power are correlated to the sawteeth crashes.

Estimates of relative power radiated by the dominant impurity species in the plasma obtained by spectroscopic measurements are also shown. The contribution of different species to the radiated power is determined by normalising VUV and XUV line intensities to the bolometric data (Lawson et al, 1990). The difference in the bolometric radiated power and the total sum of the impurity radiated power during the X-point phase (8.5-12.5 s) is due to the contribution of X-point to the radiation which is not included in the spectroscopic data as the spectroscopic cameras do not view the X-point region. A major fraction of the power is radiated by Ni and C which are of the same order of magnitude. Note that the X-point target tiles are made out of graphite which contribute to the carbon impurity in the plasma. The main original source of Ni is the antenna screen. But, there is a recirculation of Ni from screen to limiters, to X-point tiles etc. by deposition, erosion and redeposition. The actual concentration of Ni in the plasma depends on the history of the sequence of discharges on a given day. The amount of Ni influx from the screen depends on the antenna voltage, density infront of the screen, antenna phasing etc. In this discharge, the antenna was in the dipole phasing which produces less Ni impurity flux as compared to the monopole phasing (Bures et al, 1989). Thus a part of Ni comes from the antenna screen and a part from the recirculation (deposition, erosion) of Ni at other first wall surfaces. The power radiated by Be is small in the X-point phase (8.5-12.5) as the plasma does not touch the Be belt limiters. However, due to Be gettering effect, the power radiated by oxygen is negligible. The power radiated by chlorine is also negligible during the X-point phase (8.5-12.5 s) but starts to become significant during the limiter phase for $t > 12.5$ s (see also Lawson et al 1990).

3.0 ANTENNA COUPLING RESISTANCE:

3.1 Change of Coupling at the Transition and Generator Matching.

Due to the above mentioned steepening of the density profiles at the transition to H-modes, the scrape-off length of the edge plasma decreases and the density at the edge falls off more rapidly than in the L-phase. The consequence of which is that there is a sudden decrease of the coupling resistance at the transition (see Fig. 14). This puts a severe burden on the antenna matching system which has to remain tuned to continue to couple power to the plasma even with a significant variation of the load impedance on a rapid time scale (60-80 ms). Further, during the H-phase, due to heating of the plasma and changes in the plasma β (ratio of the kinetic pressure to the magnetic pressure), the plasma can drift slowly changing its distance from the antenna and causing a further change of the coupling resistance on a slower time scale (0.5-1 s). At the end of the H-phase, when the plasma reverts to the L-phase, the scrape-off length increases again and R_c increases and comes back to its L-mode value on the rapid time scale mentioned above.

In the ICRH system of JET (Wade et al, 1985), the RF power generators and the matching stubs are located at about 80 m from the antenna. Similar or even larger distances would be required in a reactor system. This long length of the transmission line is put to advantage (Jacquinot, 1984) as a small change in frequency of the generator ($\cong$ 0.25%) changes the impedance at the antenna sufficiently to bring it to a match successfully at an appropriate position of the short circuit stub. The matching of the generator is achieved by making use of two quasi-independent parameters, namely, frequency of the generator and length of the short circuit stub. These two parameters have to be varied to result finally in a perfect match. Feedback loops have been designed for both parameters. Although, the frequency of the generator can be changed on a rapid time scale (10 μs), the feedback loop of the frequency error signal is set to respond on a time scale of 10 ms (Bosia et al, 1989). The response time of the feedback loop on the stub-length error signal is determined by the movement of the mechanical stub which is about 0.3-0.5 s. Once a good match has been obtained for a given antenna load condition (either from a vacuum match condition or an L-mode plasma loading which generally can be obtained in a single shot), the

rapid changes, such as at a L-H transition, can be tracked with a fast frequency variation with a little stub movement accompanied by a small but tolerable reflection coefficient at the generator. We must point out that a fast automatic matching sytem requires a very effective generator protection systems for a rapid tripping of the generator at a fault condition otherwise it might match to an arc in the transmission line or may lead to tube failures. In JET, we are presentely implementing a new and even more powerful method of maintaining the antenna loading resistance constant throughout the ICRH pulse at a desired level by a feedback loop on the radial plasma position and the initial results are very promising.

3.2 A comparison of theory and experiment.

The coupling resistance R_c as measured experimentally in JET can be described as the value of antenna resistance seen at a current antinode of the feeder transmission line :

$$R_c = \frac{Z_{0L}}{s} \tag{2}$$

where Z_{0L} is the charcteristic impedance of the feeder line and s is the voltage standing-wave ratio. By transmission line relations, this can also be written as

$$R_c = \frac{2Z_{0L}^2 P_a}{V_{mL}^2} \tag{3}$$

where P_a is the applied RF power (forward power minus the reflected power) and V_{mL} is the maximum voltage on the line. For a $\lambda/4$ antenna, R_c reduces to

$$R_c = \frac{2Z_{0L}^2 R W_y I_{mA}^2}{V_{mL}^2} \tag{4}$$

where R is the radiation resistance per unit length , W_y is the length of the antenna in the poloidal direction and I_{mA} is the maximum current in the antenna.

This equation relates the theoretically calculated quantity R, the radiation resistance per unit length (see for example Bhatnagar et al, 1982) to the experimentally measured quantity R_c. The former quantity depends on the

physical dimensions of the antenna as well as the properties of the plasma (such as plasma density, scrape-off lengths, toroidal field, operating frequency etc.) together with the antenna-plasma distance. The latter quantity not only includes the effects of R but also the circuit properties, for example, inductance and capacitance per unit length, of the line and the antenna. To model accurately the capacitive part of the antenna is generally difficult since to resonate the antenna at the desired frequency often the antenna design requires to put metallic structures at places that fall out of line of the coordinate surfaces of the model used. Therefore, we convert the theoretically calculated R to R_c by using an experimentally measured quantity i.e. the ratio of RF currents flowing in the antenna to that in the transmission line. This quantity has been measured in a test-bed in vacuum and we assume that it does not change significantly during the operation with plasma. The theoretical results are calculated by the antenna plasma coupling code BRACCO (Bhatnagar et al, 1982, Messiaen et al, 1982). We use certain parameters that are measured experimentally such as plasma density and its profile, density scrape-off length, the antenna-plasma distance etc. Other parameters such as frequency of operation, toroidal-field and its profile, dimensions of the antenna and the mode of phasing of the antenna are used as specified in the experiment. The theoretical values were calculated at certain time slices during the H-phase and the results are shown by solid circles in Fig. 14. The antenna was in the dipole mode and the measured scrape-off length during the H-phase was 1 cm. In this phase, theoretical values agree well with the experimentally measured coupling resistance (see Fig. 14). However, during the L-phases (before and after the H-phase) the theoretical calculated values are too low as compared to the experimental ones. These values are based on a measured scrape-off length of 2.5 cm together with the other corresponding experimental data used in the calculation. The reason for this discrepancy is not well understood but we suspect that the measured scrape-off length may be in error as they are not measured directly at the antenna but are estimated from the measurements carried out at the top of the machine near the X-point and transformed to midplane. Further, only ion saturaion currents were measured by the Langmuir probes and data of the electron temperature in the scrape-off was not available which is required for getting the edge density profile. On further calculation, we find that the measured coupling resistance can be well reproduced if we simply take the SOL to be 6 cm in the L-phases of the discharge. However, a definite proof that SOL is indeed as long as 6 cm in the L-phase of such discharges must await further measurements of the density profile in front of the antenna.

4.0 DISCUSSION AND CONCLUSIONS :

Successful attempts to produce H-modes in the JET tokamak with ICRH alone eluded for some time. The main problem had been the enhanced influx of neutrals and that of metallic nickel impurities from the screen of the ICRH antenna. In the early experiments carried out with carbonized antenna, the plasma edge was perturbed by the neutral influx. With helium conditioning of the tokamak, in some discharges where H-mode signatures were just tending to appear, the H-modes were terminated rapidly by increased radiated power from the nickel impurity in the discharge. Further, it was earlier believed that the plasma had to be kept some distance away from any material surface for producing good H-modes. This tended one to use the monopole configuration of the antenna for coupling any significant power when the plasma is more than 5 cm away from the side-protection tiles of the antenna. Monopole is known to produce enhanced impurity influx as compared to dipole. Dipole was also tried but power sufficient for achieving an H-mode could not be coupled. Attempts to bring plasma closer to the antenna lead to further increase in impurity and neutral particle influx. By the operation of ICRH in the NBI H-modes, it was also clear that at the rapid L-H transition, the coupling drops due to steepening of the density profile and the generator mismatches due to the change of antenna loading causing breakdown in the antenna and the transmission line. As mentioned in the introduction, Be-evaporation reduced the oxygen concentration due to its gettering effect, reduced the ICRH specific impurity-influx from the antenna as the self-sputtering coefficient of Be is less than unity, and also reduced the neutral influx due to pumping action of Be-coated surfaces. This allowed the plasma to be brought closer ($\cong$ 2 cm) and dipole to be used. Automatic matching systems largely eliminated the problem of mismatch at a L-H transition. A combination of these improvements allowed us to achieve long ICRH H-mode successfully in JET.

In some discharges with ICRH, we have found a clear H-mode like confinement but a drop in the D_α-signal was not observed. This effect could be related to the very small ($\cong$ 1 cm) distance that was used in these discharges. Similar effect was also found in some combined ICRH + NBI heating H-modes (Tubbing et al, 1989b). In some shots with ICRH alone, several transitions from L to H-mode and then back to L-mode are observed (Tubbing et al, 1989a). Each L-H transition has the usual signatures. Each H-phase is terminated when the radiated power approaches the input power. During the L-phase, the radiated

power becomes smaller due to reduced density and lesser impurity accumulation and then the next L-H transition occurs. Similar behaviour has also been found in both NBI and combined ICRH + NBI discharges (Bhatnagar et al, 1987).

In general, in ELM-free H-modes, due to the increased particle and impurity confinement, the density continues to rise strongly and the H-mode is terminated when the radiated power exceeds the input power. This limits the duration of H-mode. There is some contribution to this increased particle density in the case of NBI heating by fueling in the centre by the neutral beam itself whereas in the case with ICRH, there is no such fueling especially in the Be-gettered environment. However, the effect of particle confinement dominates in the increase of plasma density. H-modes can be made longer by ejecting particles periodically, for example, by provoking ELMs (Gohil et al, 1989). However, H-modes made longer in this way often suffer from some degradation in energy confinement time. H-modes in JET with NBI have been produced for longer than 5 s (Stork et al, 1990). Efforts are being made to obtain even longer or quasi steady-state H-modes in JET.

In conclusion, ICRH produced H-mode discharges in JET are found to have the same characteristics as those produced by NBI or combined ICRH + NBI heating. The global confinement time in ICRH H-mode discharges (as in NBI or combined ICRH + NBI discharges) approaches two-times Goldston L-mode prediction. A local transport analysis shows that effective heat conductivity in ICRH H-mode discharges decreases in the edge plasma region which could be related to the steepening of the edge density profile. A characteristic feature of ICRH, the monster sawtooth remains uninterrupted at the L-H transition and the stabilization of the sawtooth is maintained during the H-phase of the discharge leading to $T_{e0} = 10$ keV nearly twice the value of T_{i0}. Combined heating H-modes, push both T_{e0} and T_{i0} close to 10 keV simultaneously. The increase of T_{e0} in such a case allows to increase the slowing down time of the beam ions and leads to higher D-D reaction rates and neutron output. For most of their duration ICRH H-modes are found to be free from ELMs (edge localised modes). ICRH H-modes often occur as a two-step transition and R_c also decreases in two steps. Theoretical values of R_c agree well with experimental values during the H-phase. Finally, the beryllium evaporation on the antenna screen and the tokamak first wall, a physical understanding of the release of impurity influx from the powered ICRH antenna and the implementation of a rapid automatic antenna matching system have played a crucial role in achieving clear H-modes in the JET tokamak with ICRH alone. This increasingly indicates that all plasma heating methods in a tokamak are essentially similar in their performance of the global energy confinement and has lead to an increased optimism that the α-particle heating in a reacting plasma will also be similar although a final assesement would only come from experiments in the D-T phase of JET and those in the next-step devices.

5.0 ACKNOWLEDGEMENT :

We wish to thank our colleagues in the JET team, especially the RF plant team, the NBI team, the tokamak operation team and those operating the diagnostics used in the experiments reported in this paper.

6.0 REFERENCES :

(1) AKIBA M., et al., (1988) Plasma Physics Controlled Fusion, 30, 1405.
(2) ASDEX TEAM, (1989) Nuclear Fusion, 29, 1959.
(3) BALET, B. et al., (1990) Proc 17th European Conference on Controlled Fusion and Plasma Heating, Amsterdam, Holland, (1990) Europhysics Conf. Abstracts, vol 14B, part I, 162.
(4) BHATNAGAR, V.P. et al., (1982) Nucl. Fusion, 22, 280.
(5) BHATNAGAR, V.P. et al., (1984) Nucl. Fusion, 24, 955.
(6) BHATNAGAR, V.P. et al., (1987) Bull. American Phys. Soc., Series II, 32, 1837; see also Report JET-IR(87)18, JET Joint Undertaking, Abingdon, OXON, U.K.
(7) BHATNAGAR, V.P. et al., (1989a) Plasma Physics Controlled Fusion, 31, 333.
(8) BHATNAGAR, V.P. et al., (1989b) Plasma Physics Controlled Fusion, 31, 2111.
(9) BOSIA. G. et al., (1989) Fusion Technology, I, 459.
(10) BURES M. et al., (1988a) Plasma Physics Controlled Fusion, 30, 1833.
(11) BURES M. et al., (1988b) Plasma Physics Controlled Fusion, 30, 149.
(12) BURES M. et al., (1989) IAEA Technical Committee on ICRH Edge Physics, published in Fusion Engineering and Design (1990) 12, 251.
(13) CAMPBELL, D. J. et al, (1988) Phys. Rev. Lett., 60, 2148.
(14) DEUSING, D., (1986) Plasma Physics Controlled Fusion, 28, 1429.
(15) DIETZ et al, (1990) Plasma Physics Controlled Fusion, to be published.
(16) D'IPPOLITO, D.A. et al., (1989) IAEA Technical Committee on ICRH Edge Physics, published in Fusion Engineering and Design (1990) 12, 209.
(17) GOHIL, P. et al, (1989) Bull. American Phys. Society, 34, 1939.
(18) GOLDSTON, R.J. et al, (1981) J. Comput. Physics, 43, 61.
(19) GOLDSTON, R.J. (1984) Plasma Physics Controlled Fusion, 26, 87.
(20) GOWERS, C. et al., (1986) Proc 15th European Conference on Controlled Fusion and Plasma Heating, Dubrovnik, Yugoslavia, (1988) Europhysics Conf. Abstracts, vol 12B, part I, 239.
(21) ITER Team, (1989) ITER Concept Definition, ITER Documentation Series, No. 3, Vol. 1-2, International Atomic Energy Agency, Vienna 1989.
(22) JACQUINOT, J. (1984) JET Joint Undertaking, Abingdon, England, (U.K.), RF-JDN/J/83.7.

(23) JACQUINOT, J. et al (1986), Proc. IAEA Conf. on Plasma Phys. and Contr. Nuclear Fusion Research, Kyoto, Japan, Nuclear Fusion Supplement 1987, vol. 1, 449.
(24) JACQUINOT, J. (1989a), Private Communication.
(25) JACQUINOT, J. et al., (1989b) IAEA Technical Committee on ICRH Edge Physics, published in Fusion Engineering and Design (1990) 12, 245.
(26) KAYE A.S. et al (1987) Fusion Technology, 2, 203.
(27) KEILHACKER, M., et al., (1984) Proc. IAEA Conf. on Plasma Physics and Controlled Nuclear Nuclear Fusion Research, London, U.K., paper CN-44/A-II-1
(28) KEILHACKER, M. et al, (1986) Plasma Physics Controlled Fusion, 28, 29.
(29) LAZZARO, E. et al, (1987) Report JET-P(87)58, JET Joint Undertaking, Abingdon, U.K.
(30) LAWSON, K.D. et al., (1990) Proc 17th European Conference on Controlled Fusion and Plasma Heating, Amsterdam, Holland, (1990) Europhysics Conf. Abstracts, vol 14b, part III, 1413.
(31) MATSUMOTO, H. et al., (1987) Nucl. Fusion, 27, 1181.
(32) McCARTHY, L. et al., (1990) Proc 15th European Conference on Controlled Fusion and Plasma Heating, Dubrovnik, Yugoslavia, (1988) Europhysics Conf. Abstracts vol 12b, part II, 717.
(33) MESSIAEN, A.M. et al., (1982) Proc. 3rd Joint Grenoble-Varenna International Symposium, Grenoble, France, vol. 1, 243.
(34) MESSIAEN, A.M. et al, (1989) Plasma Physics Controlled Fusion, 31, 930.
(35) MYRA J.R. et al., (1989) Report No. LRC-89-5, Lodestar Research Corporation, Boulder, Colorado, 80310, U.S.A.
(36) OHYABU, N. et al., (1985) Nucl. Fusion, 25, 49.
(37) ORLINSKIJ D.V. and MAGYAR G. (1988) Nucl. Fusion, 28, 611.
(38) PERKINS F.W., (1989) Nucl. Fusion, 29, 583.
(39) PRENTICE, R. et al, et al., (1990) Proc 17th European Conference on Controlled Fusion and Plasma Heating, Amsterdam, Holland, (1990) Europhysics Conf. Abstracts, vol 14b, part IV, 1500.
(40) REBUT P.H. et al, (1984) Proc. IAEA Conf. on Plasma Physics and Controlled Nuclear Fusion Research, London, England, Nuclear Fusion supplement 1985, vol. 1, 11.
(41) ROTH J., (1987) J. Nucl. Mat. 145-147, 87.
(42) SADLER, G. et al., (1990) Proc 17th European Conference on Controlled Fusion and Plasma Heating, Amsterdam, Holland, (1990) Europhysics Conf. Abstracts, vol 14b, part I, 1.
(43) STEINMETZ, K. et al., (1987) Phys. Rev. Lett. 58, 124.
(44) STEINMETZ, K. et al., (1986) Proc 13th European Conference on Controlled Fusion and Plasma Heating, Schlierse, Germany, (1986) Europhysics Conf. Abstracts, vol 10C, part II, 21.
(45) STEVENS J.E. et al, (1990) Plasma Physics Controlled Fusion, 32, 189.

(46) STORK D. et al, (1990) 9th Int. Conf. on Plasma Surface Interaction in Controlled Fusion Devices, Bournemouth, (U.K.), paper P:25, to be published in J. of Nuclear Materials.
(47) TAMAI, H. et al, (1986) Nucl. Fusion, 26, 365.
(48) TANGA, A. et al., (1986) Proc. IAEA Conf. on Plasma Physics and Controlled Nuclear Nuclear Fusion Research, Kyoto, Japan, Nuclear Fusion Supplement, 1987 Vol. 1, 65.
(49) TUBBING, B.J.D. et al., (1989a) Proc 16th European Conference on Controlled Fusion and Plasma Heating, Venice, Italy, (1989) Europhysics Conf. Abstracts, vol 13b, part I, 237.
(50) TUBBING, B.J.D. et al, (1989b) Nucl. Fusion, 29, 1953.
(51) WADE T. et al (1985) Proc. 11th Symposium on Fusion Engineering, Austin, Texas.
(52) WAGNER, F. et al., (1982) Phys. Rev. Letters, 49, 1408.

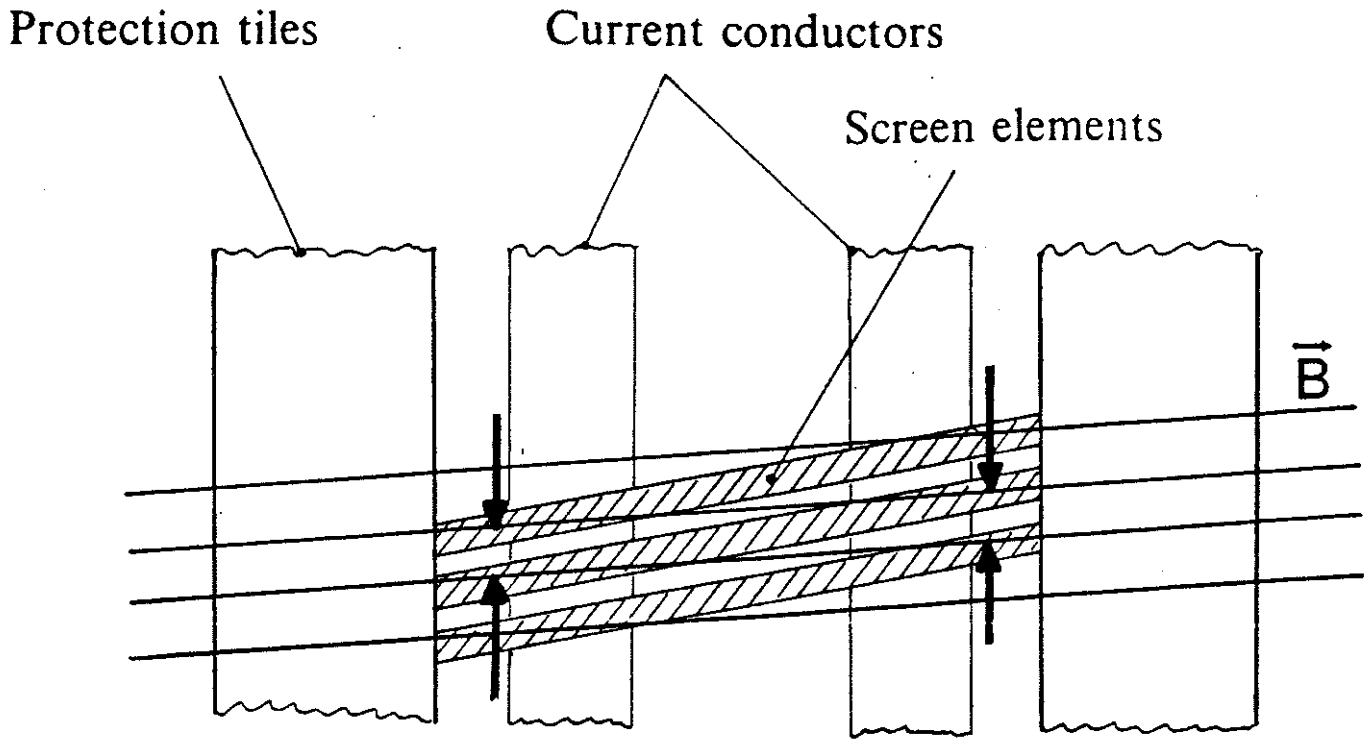

FIG. 1 (a). A schematic drawing of the front view of a JET ICRH antenna seen from the plasma. The arrows indicate the closure of the electrical circuit at the screen gaps by the B-field line (short length gap-sheaths)

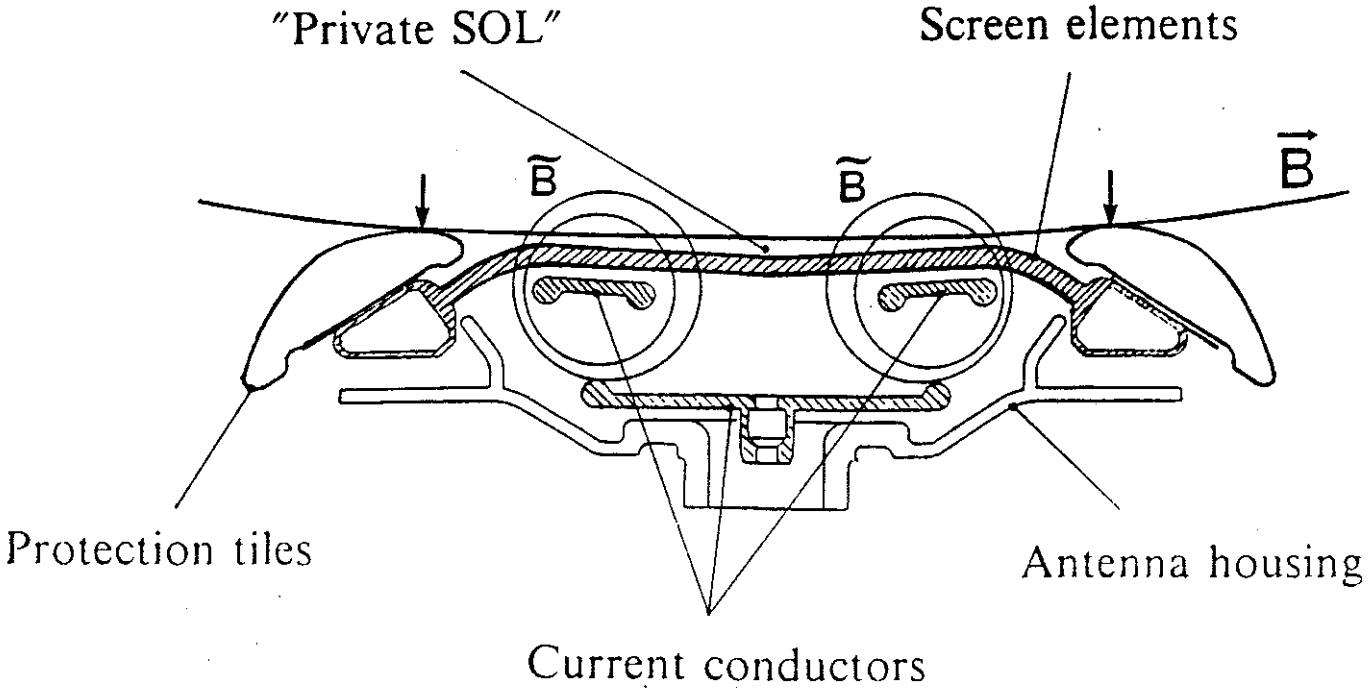

FIG. 1 (b). A cross sectional view at the midplane of the JET A1-antenna. Again the arrows indicate the closure of the electrical circuit at the side-protection tiles and similarly at the screen rods on the two sides of the antenna central conductors (long-length front-surface sheaths)

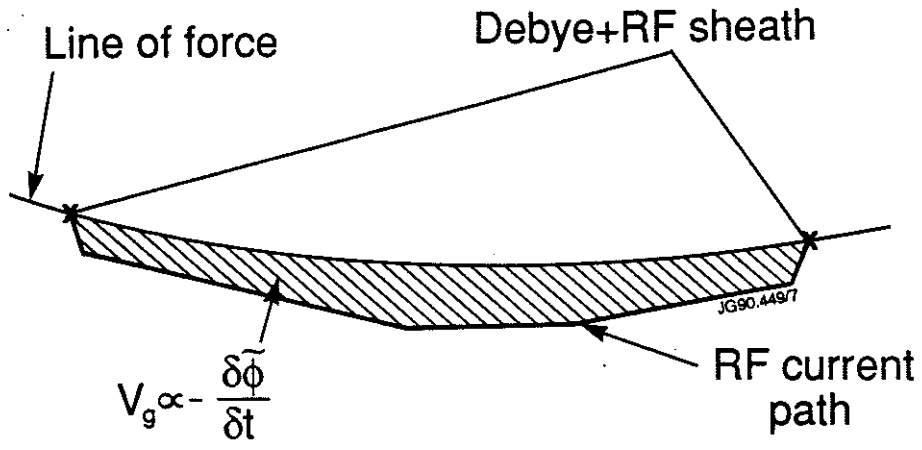

FIG. 2. A schematic drawing of the electrical circuit in the RF sheath rectification process.

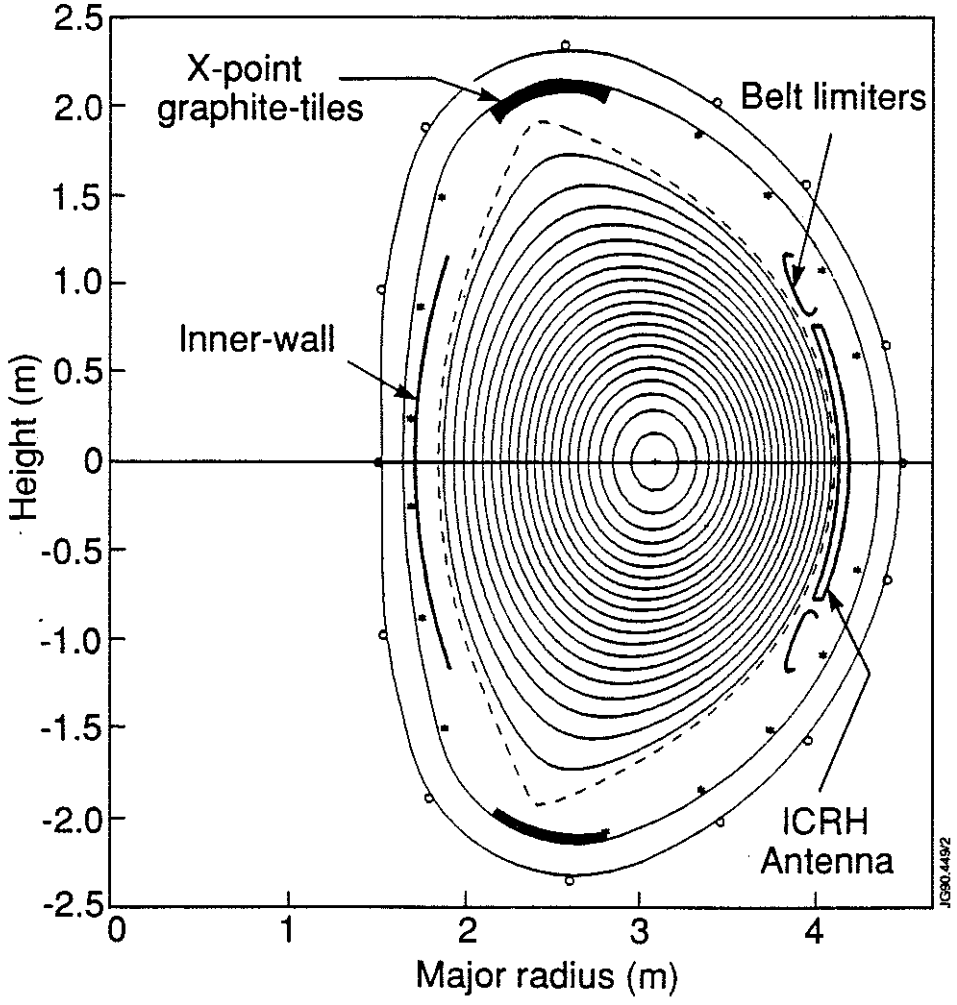

FIG. 3. Poloidal-flux contours computed from the IDENTC equilibrium code showing the double-null X-point configuration for an ICRH H-mode plasma.

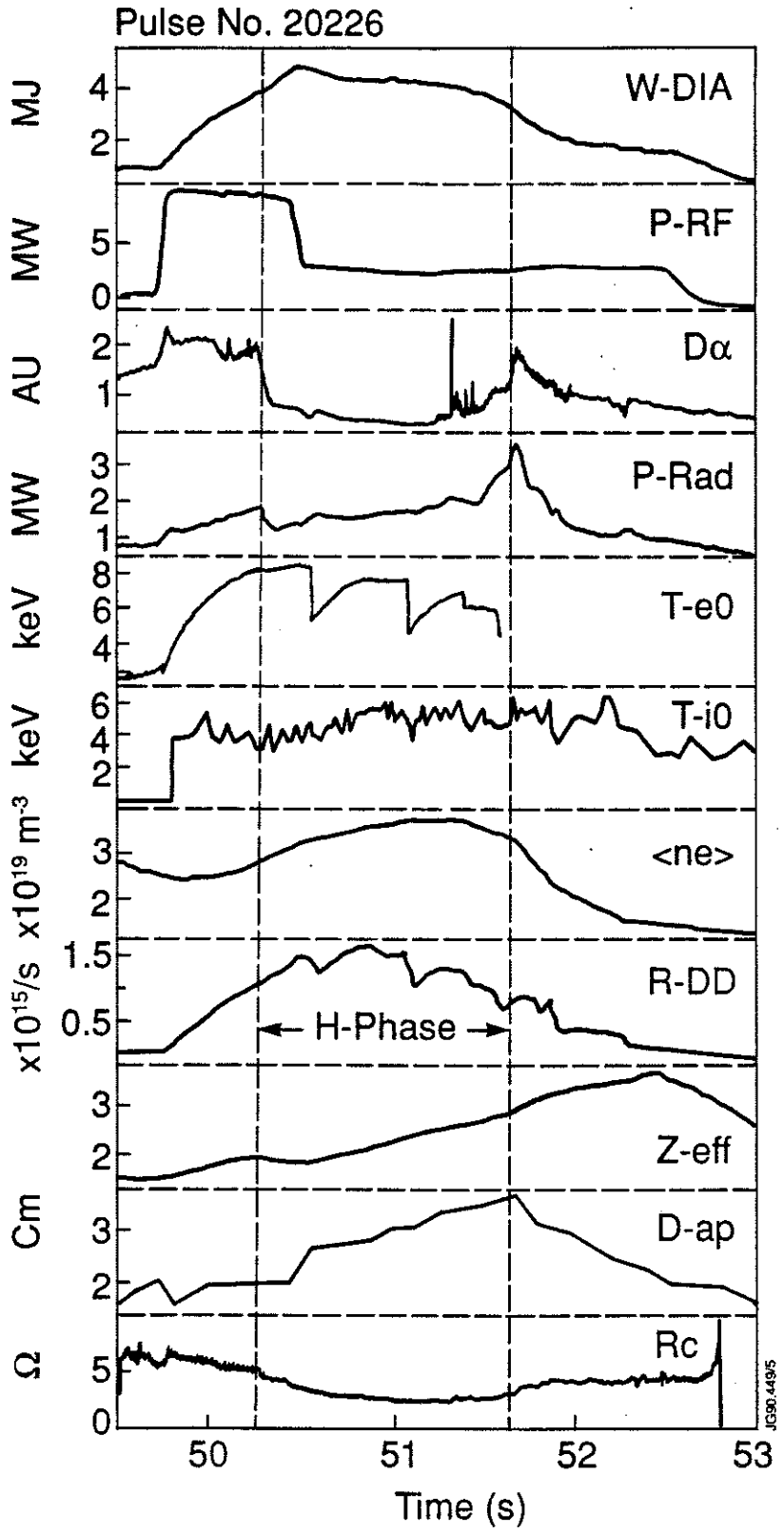

FIG. 4. Time traces for an H-mode discharge with ICRH alone.

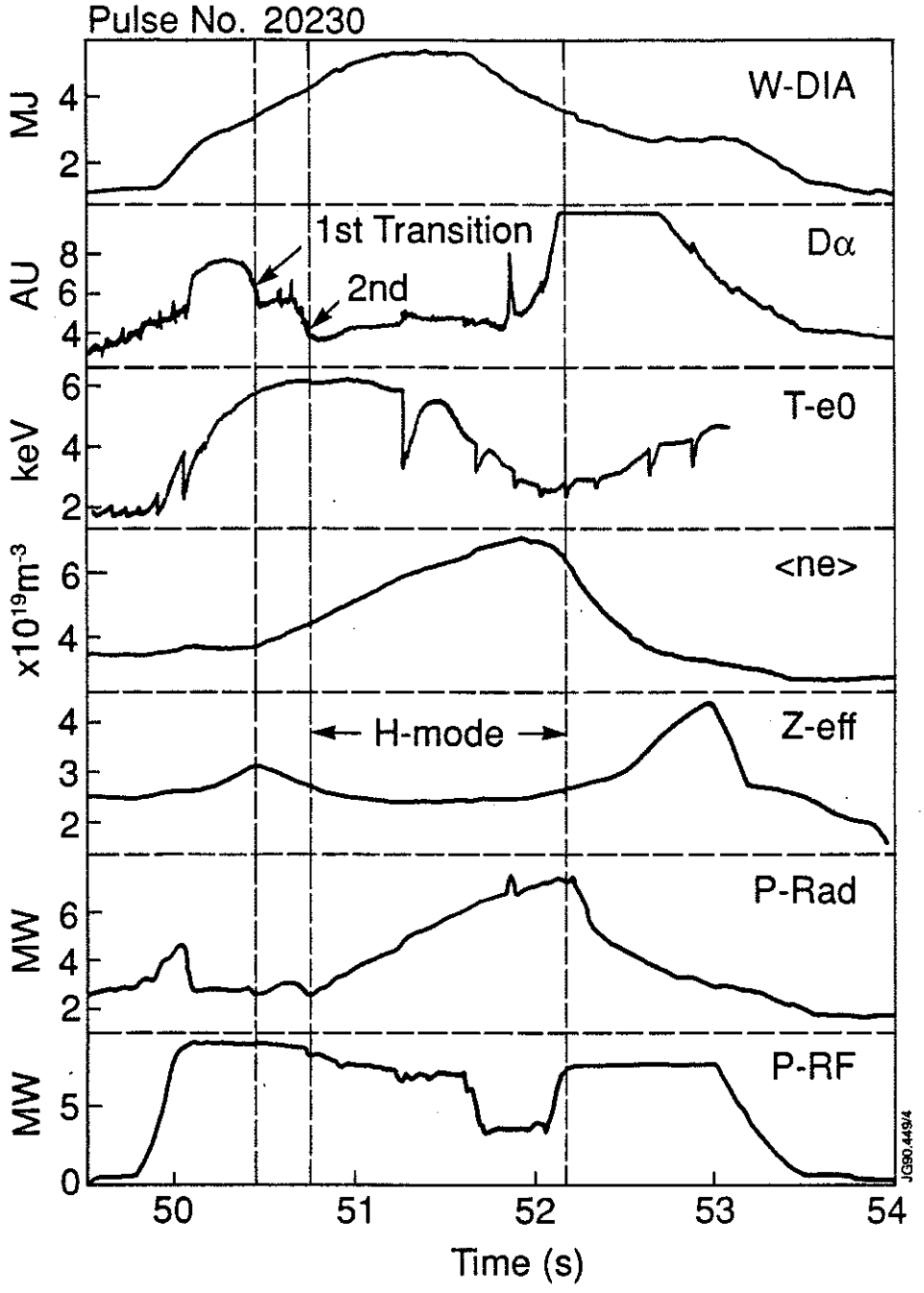

FIG. 5. Time traces of an ICRH H-mode with a two-step transition.

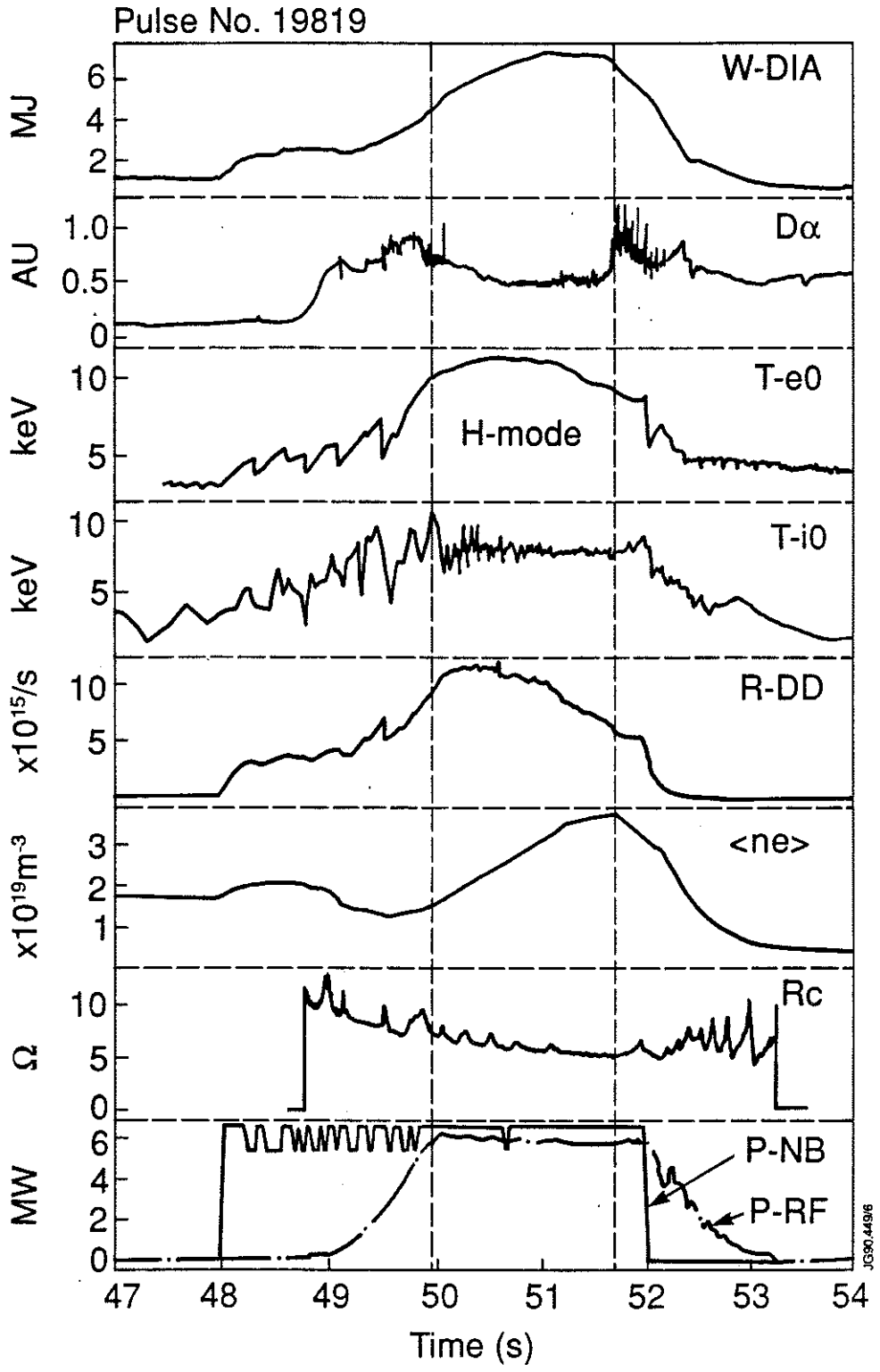

FIG. 6. Time traces for an H-mode discharge with combined ICRH + NBI heating.

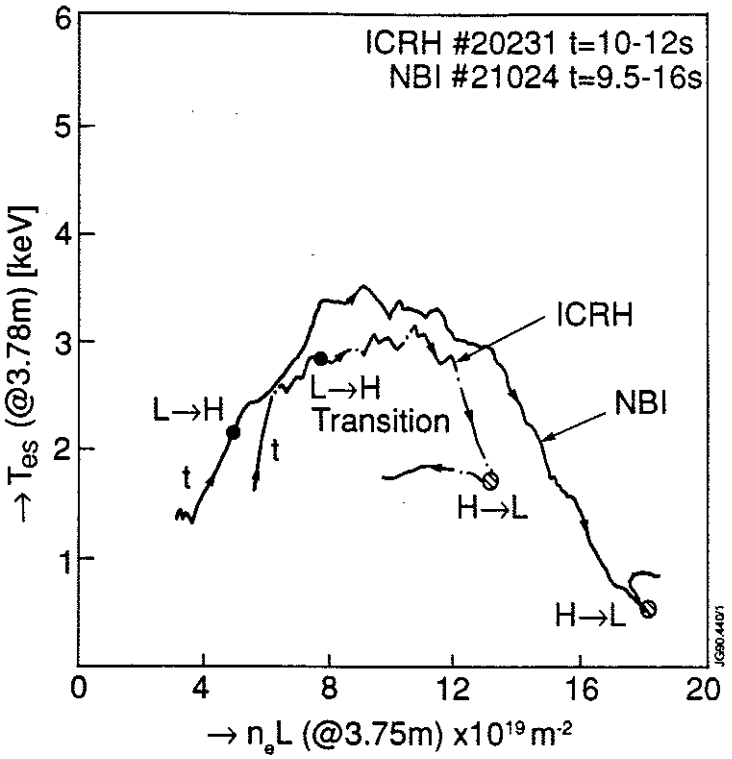

FIG. 7. Evolution of edge-temperature vs edge-density in an ICRH H-mode, and an NBI H-mode discharge in JET where time is the parameter along the trace. Note that R = 3.75 m refers to a distance of about 30 cm from the edge of the plasma.

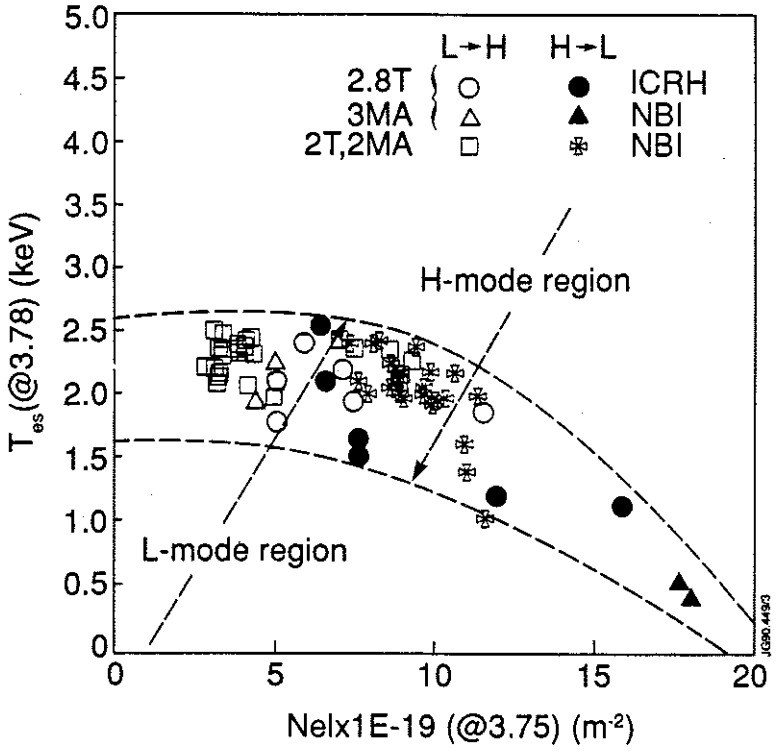

FIG. 8. A plot of edge temperature vs edge-density at the L-H and H-L transition of many shots of JET featuring an H-mode obtained with ICRH or NBI. Also, see the remark in Fig. 7.

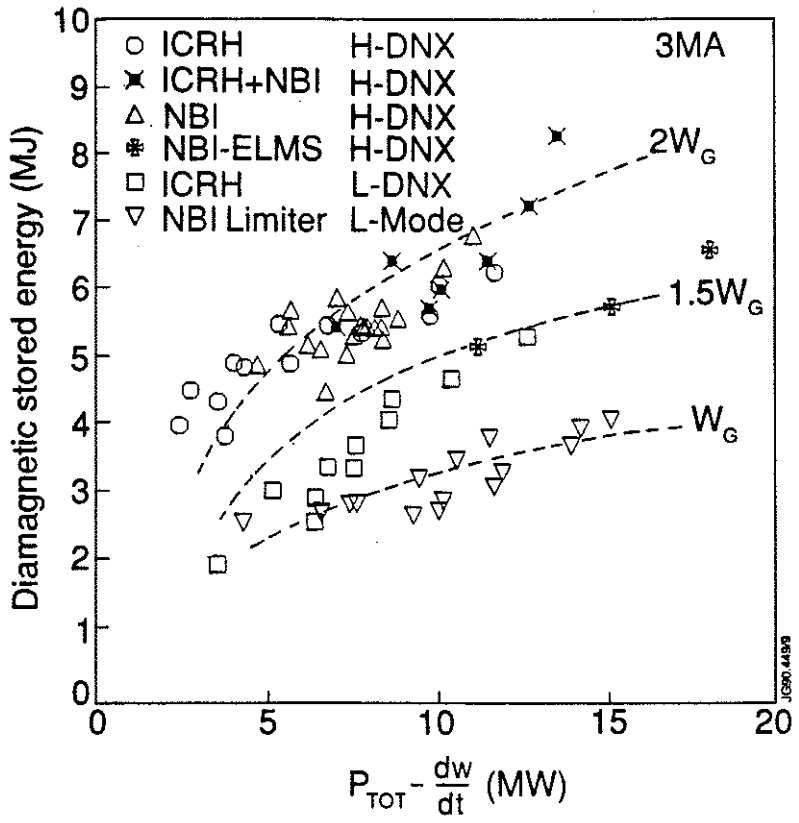

FIG. 9. A plot of diamagnetic stored energy W as a function of P_T-dW/dt for several scenarios of additional heating in JET. W_G represents the Goldston L-mode prediction for such discharges.

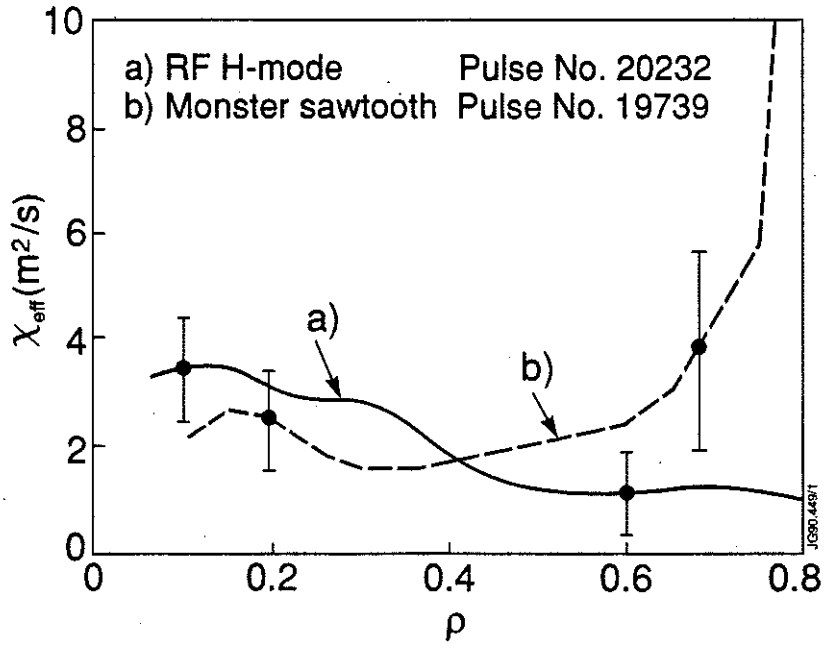

FIG. 10. A TRANSP calculated plot of "effective" (see Eq. 1) thermal diffusivity as a function of the normalized radius for an ICRH H-mode (during the H-phase) and an ICRH L-mode featuring a monster sawtooth (during the monster sawtooth phase).

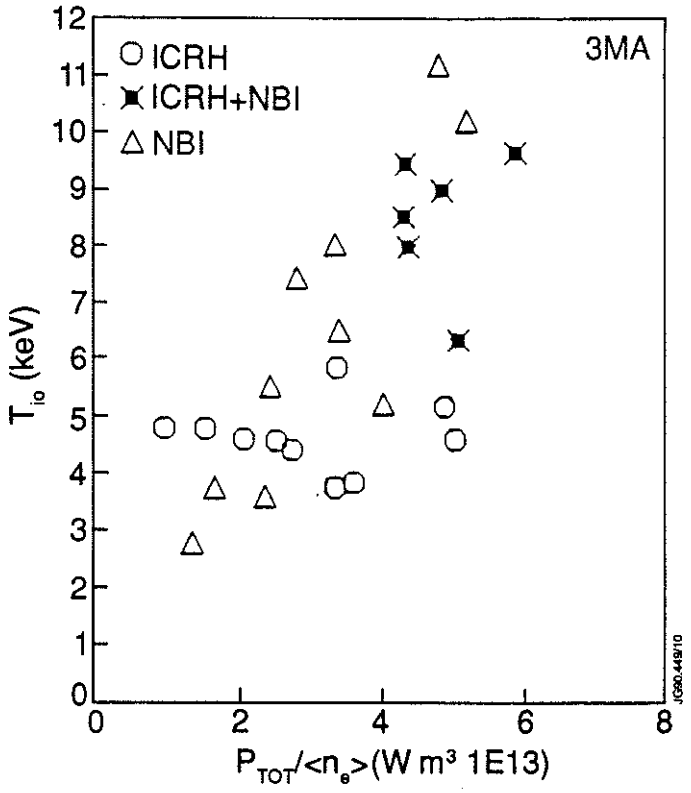

FIG. 11. A plot of central ion temperature vs $P_{TOT}/<n_e>$, for several H-mode scenarios in JET, where P_{TOT} is the total input power and $<n_e>$ is the volume average density.

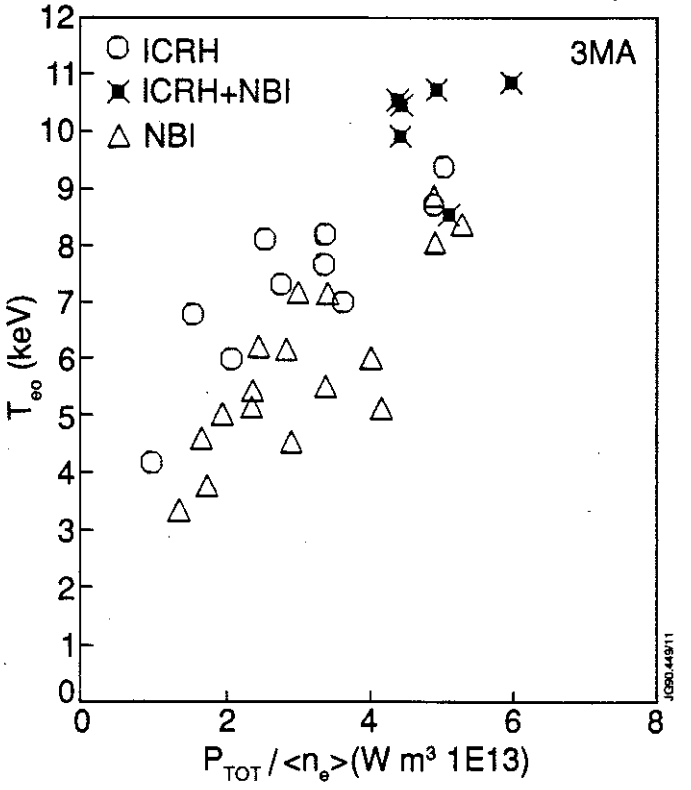

FIG. 12. A plot of central electron temperature vs $P_{TOT}/<n_e>$, for several H-mode scenarios in JET, where P_{TOT} is the total input power and $<n_e>$ is the volume average density.

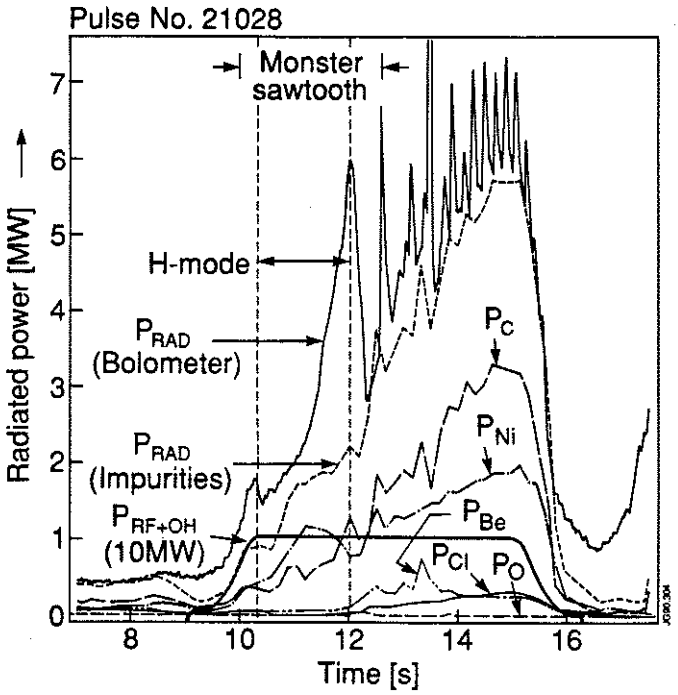

FIG. 13. A plot of radiated power from the plasma as a function of time for an ICRH H-mode. The total radiated power is obtained from the bolometric measurements which includes the radiation from X-point. Also shown are the relative contributions of dominant impurity species to the radiated power based on VUV and XUV spectroscopy which does not view the X-point. The duration of the X-point phase is from 8.5-12.5 s. In this figure, on the X-axis 40 s have been subtracted to make t=0 to coincide with the start of the plasma current as opposed to some other figures where actual time sequence was used.

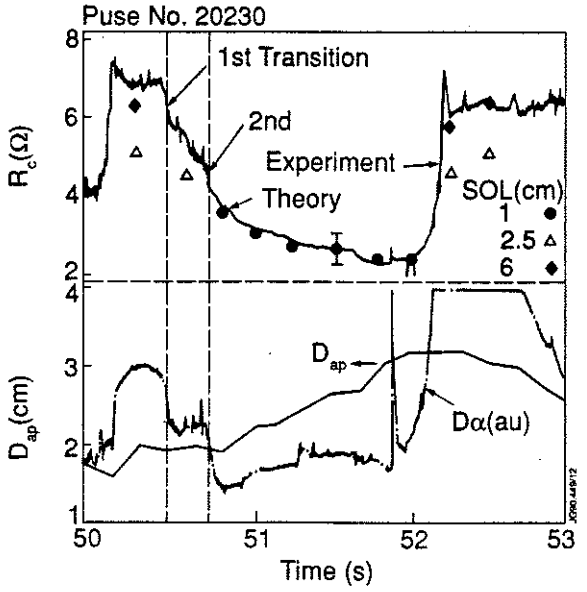

FIG 14. A time trace of experimentally measured antenna coupling resistance R_c, the vertical $D\alpha$-emission and the plasma separatrix to antenna side protection distance for an ICRH H-mode with a two step transition. Also shown are the theoretically calculated values of R_c at a number of time slices using some experimental data as input. The error bar on the theoretical results reflect the uncertainty on the measured value of SOL used in these calculations. In the L-phase results are also shown when SOL is taken to be 6 cm whereas experimentally estimated SOL was about 2.5 cm.

APPENDIX 1.

THE JET TEAM

JET Joint Undertaking, Abingdon, Oxon, OX14 3EA, U.K.

J.M.Adams[1], F.Alladio[4], H.Altmann, R.J.Anderson, G.Appruzzese, W.Bailey, B.Balet, D.V.Bartlett, L.R.Baylor[24], K.Behringer, A.C.Bell, P.Bertoldi, E.Bertolini, V.Bhatnagar, R.J.Bickerton, A.Boileau[3], T.Bonicelli, S.J.Booth, G.Bosia, M.Botman, D.Boyd[31], H.Brelen, H.Brinkschulte, M.Brusati, T.Budd, M.Bures, T.Businaro[4], H.Buttgereit, D.Cacaut, C.Caldwell-Nichols, D.J.Campbell, P.Card, J.Carwardine, G.Celentano, P.Chabert[27], C.D.Challis, A.Cheetham, J.Christiansen, C.Christodoulopoulos, P.Chuilon, R.Claesen, S.Clement[30], J.P.Coad, P.Colestock[6], S.Conroy[13], M.Cooke, S.Cooper, J.G.Cordey, W.Core, S.Corti, A.E.Costley, G.Cottrell, M.Cox[7], P.Cripwell[13], F.Crisanti[4], D.Cross, H.de Blank[16], J.de Haas[16], L.de Kock, E.Deksnis, G.B.Denne, G.Deschamps, G.Devillars, K.J.Dietz, J.Dobbing, S.E.Dorling, P.G.Doyle, D.F.Düchs, H.Duquenoy, A.Edwards, J.Ehrenberg[14], T.Elevant[12], W.Engelhardt, S.K.Erents[7], L.G.Eriksonn[5], M.Evrard[2], H.Falter, D.Flory, M.Forrest[7], C.Froger, K.Fullard, M.Gadeberg[11], A.Galetsas, R.Galvao[8], A.Gibson, R.D.Gill, A.Gondhalekar, C.Gordon, G.Gorini, C.Gormezano, N.A.Gottardi, C.Gowers, B.J.Green, F.S.Griph, M.Gryzinski[26], R.Haange, G.Hammett[6], W.Han[9], C.J.Hancock, P.J.Harbour, N.C.Hawkes[7], P.Haynes[7], T.Hellsten, J.L.Hemmerich, R.Hemsworth, R.F.Herzog, K.Hirsch[14], J.Hoekzema, W.A.Houlberg[24], J.How, M.Huart, A.Hubbard, T.P.Hughes[32], M.Hugon, M.Huguet, J.Jacquinot, O.N.Jarvis, T.C.Jernigan[24], E.Joffrin, E.M.Jones, L.P.D.F.Jones, T.T.C.Jones, J.Källne, A.Kaye, B.E.Keen, M.Keilhacker, G.J.Kelly, A.Khare[15], S.Knowlton, A.Konstantellos, M.Kovanen[21], P.Kupschus, P.Lallia, J.R.Last, L.Lauro-Taroni, M.Laux[33], K.Lawson[7], E.Lazzaro, M.Lennholm, X.Litaudon, P.Lomas, M.Lorentz-Gottardi[2], C.Lowry, G.Magyar, D.Maisonnier, M.Malacarne, V.Marchese, P.Massmann, L.McCarthy[28], G.McCracken[7], P.Mendonca, P.Meriguet, P.Micozzi[4], S.F.Mills, P.Millward, S.L.Milora[24], A.Moissonnier, P.L.Mondino, D.Moreau[17], P.Morgan, H.Morsi[14], G.Murphy, M.F.Nave, M.Newman, L.Nickesson, P.Nielsen, P.Noll, W.Obert, D.O'Brien, J.O'Rourke, M.G.Pacco-Düchs, M.Pain, S.Papastergiou, D.Pasini[20], M.Paume[27], N.Peacock[7], D.Pearson[13], F.Pegoraro, M.Pick, S.Pitcher[7], J.Plancoulaine, J-P.Poffé, F.Porcelli, R.Prentice, T.Raimondi, J.Ramette[17], J.M.Rax[27], C.Raymond, P-H.Rebut, J.Removille, F.Rimini, D.Robinson[7], A.Rolfe, R.T.Ross, L.Rossi, G.Rupprecht[14], R.Rushton, P.Rutter, H.C.Sack, G.Sadler, N.Salmon[13], H.Salzmann[14], A.Santagiustina, D.Schissel[25], P.H.Schild, M.Schmid, G.Schmidt[6], R.L.Shaw, A.Sibley, R.Simonini, J.Sips[16], P.Smeulders, J.Snipes, S.Sommers, L.Sonnerup, K.Sonnenberg, M.Stamp, P.Stangeby[19], D.Start, C.A.Steed, D.Stork, P.E.Stott, T.E.Stringer, D.Stubberfield, T.Sugie[18], D.Summers, H.Summers[20], J.Taboda-Duarte[22], J.Tagle[30], H.Tamnen, A.Tanga, A.Taroni, C.Tebaldi[23], A.Tesini, P.R.Thomas, E.Thompson, K.Thomsen[11], P.Trevalion, M.Tschudin, B.Tubbing, K.Uchino[29], E.Usselmann, H.van der Beken, M.von Hellermann, T.Wade, C.Walker, B.A.Wallander, M.Walravens, K.Walter, D.Ward, M.L.Watkins, J.Wesson, D.H.Wheeler, J.Wilks, U.Willen[12], D.Wilson, T.Winkel, C.Woodward, M.Wykes, I.D.Young, L.Zannelli, M.Zarnstorff[6], D.Zasche[14], J.W.Zwart.

PERMANENT ADDRESS

1. UKAEA, Harwell, Oxon. UK.
2. EUR-EB Association, LPP-ERM/KMS, B-1040 Brussels, Belgium.
3. Institute National des Récherches Scientifique, Quebec, Canada.
4. ENEA-CENTRO Di Frascati, I-00044 Frascati, Roma, Italy.
5. Chalmers University of Technology, Göteborg, Sweden.
6. Princeton Plasma Physics Laboratory, New Jersey, USA.
7. UKAEA Culham Laboratory, Abingdon, Oxon. UK.
8. Plasma Physics Laboratory, Space Research Institute, Sao José dos Campos, Brazil.
9. Institute of Mathematics, University of Oxford, UK.
10. CRPP/EPFL, 21 Avenue des Bains, CH-1007 Lausanne, Switzerland.
11. Risø National Laboratory, DK-4000 Roskilde, Denmark.
12. Swedish Energy Research Commission, S-10072 Stockholm, Sweden.
13. Imperial College of Science and Technology, University of London, UK.
14. Max Planck Institut für Plasmaphysik, D-8046 Garching bei München, FRG.
15. Institute for Plasma Research, Gandhinagar Bhat Gujat, India.
16. FOM Instituut voor Plasmafysica, 3430 Be Nieuwegein, The Netherlands.
17. Commissiariat à L'Energie Atomique, F-92260 Fontenay-aux-Roses, France.
18. JAERI, Tokai Research Establishment, Tokai-Mura, Naka-Gun, Japan.
19. Institute for Aerospace Studies, University of Toronto, Downsview, Ontario, Canada.
20. University of Strathclyde, Glasgow, G4 ONG, U.K.
21. Nuclear Engineering Laboratory, Lapeenranta University, Finland.
22. JNICT, Lisboa, Portugal.
23. Department of Mathematics, Univeristy of Bologna, Italy.
24. Oak Ridge National Laboratory, Oak Ridge, Tenn., USA.
25. G.A. Technologies, San Diego, California, USA.
26. Institute for Nuclear Studies, Swierk, Poland.
27. Commissiariat à l'Energie Atomique, Cadarache, France.
28. School of Physical Sciences, Flinders University of South Australia, South Australia SO42.
29. Kyushi University, Kasagu Fukuoka, Japan.
30. Centro de Investigaciones Energeticas Medioambientales y Techalogicas, Spain.
31. University of Maryland, College Park, Maryland, USA.
32. University of Essex, Colchester, UK.
33. Akademie de Wissenschaften, Berlin, DDR.

CR 88.49.1A